Gaia21blx: complete resolution of a binary microlensing event in the Galactic disk

Astronomy & Astrophysics manuscript no. output
March 30, 2024

Gaia21blx: complete resolution of a binary microlensing event in the Galactic disk

P. Rota[1,2], V. Bozza[1,2], M. Hundertmark[3]
and
E. Bachelet[9], R. Street[4], Y. Tsapras[3], A. Cassan[8], M. Dominik[5], R. Figuera Jaimes[6,7], K. A. Rybicki[11], J. Wambsganss[3], Ł. Wyrzykowski[10], P. Zieliński[12]
The OMEGA Key Project
and
M. Bonavita[21], T. C. Hinse[22], U. G. Jørgensen[13], E. Khalouei[15], H. Korhonen[13], P. Longa-Peña[17], N. Peixinho[16], S. Rahvar[18], S. Sajadian[14], J. Skottfelt[20], C. Snodgrass[21], and J. Tregolan-Reed[19]
The MiNDSTEp consortium

(Affiliations can be found after the references)

Received ??; accepted ??

ABSTRACT

Context. Gravitational microlensing is a method used to discover planet-hosting systems at distances of several kpc, in the Galactic disk and bulge. Here we present the analysis of a microlensing event alerted by the Gaia photometric alert team with a possibly bright lens.
Aims. In order to infer the mass and distance to the lensing system, the parallax measurement at the position of Gaia21blx is used. In this particular case, the source and the lens have comparable magnitudes and we cannot attribute the parallax measured by Gaia to the lens or source alone.
Methods. Since the blending flux is important, we assume that the Gaia parallax is the flux-weighted average of the parallaxes of lens and source. Combining this assumption with the information from the microlensing models and the finite source effects we are able to resolve all degeneracies, thus obtaining, mass, distance, luminosities and projected kinematics of the binary lens and the source.
Results. According to the best model, the lens is a binary system 2.18 ± 0.07 kpc from Earth composed of a G star of $0.95 \pm 0.17\ M_\odot$ and a K star of $0.53 \pm 0.07\ M_\odot$. The source is likely to be an F subgiant star at 2.38 ± 1.71 kpc with a mass of $1.10 \pm 0.18\ M_\odot$. Both lenses and the source follow the kinematics of the thin disk population. We also discuss alternative models, which are disfavored by the data or by prior expectations.

Key words. lensing:micro — Binaries

1. Introduction

Gravitational microlensing occurs when the light of the background source star is deflected by a foreground object (called lens). The result is a time-variable magnification of the flux signal and from the study of the shape of the light curve we can determine the properties of the lens (Mao 2012; Gaudi 2012; Tsapras 2018). This phenomenon was first theorized by Einstein (1936), and Paczyński (1986) described how to apply the method to find dark matter in the Galactic halo. In recent years, microlensing has become a unique tool for the identification of planets around faint objects, planets that otherwise could not be detected with other techniques. In particular, with gravitational microlensing we can study binary systems irrespective of the luminosity of their components, since it is the result of their gravitational influence on the light of a background source that is detected, not their intrinsic luminosity; in this way we are able to find exoplanets orbiting single or binary stars (Gould & Loeb 1992; Bond et al. 2004; Bennett et al. 2016), brown dwarfs (Bozza et al. 2012; Ranc et al. 2015; Herald et al. 2022) or compact objects such as black holes or stellar remnants (Shvartzvald et al. 2015; Wyrzykowski et al. 2016; Sahu et al. 2022; Lam et al. 2022; Mróz et al. 2022).

There are numerous surveys carried out by various collaborations such as OGLE (Udalski 2003), MOA (Bond et al. 2001; Sumi et al. 2003) and KMTNet (Kim et al. 2016) as well as follow-up teams such as μFun (Gould 2008), PLANET (Albrow et al. 1998), RoboNet (Tsapras et al. 2009), MiNDSTEp (Dominik et al. 2010) and the OMEGA Key Project (Bachelet et al. in prep.).
With the new generation of large-sky surveys we are able to find microlensing events in the entire sky. And for this purpose the work of Gaia is of fundamental importance given its mission to build an extremely detailed three-dimensional map of the Milky Way (Gaia Collaboration et al. 2016). It is worth noting that historically, microlensing discoveries have been confined to a small region in the Bulge, in contrast to Gaia's probing of the whole galaxy. Gaia's early alerting capabilities (Hodgkin et al. 2021) played a crucial role in obtaining timely follow-up observations for many important microlensing events discovered by the mission (Gaia Collaboration et al. 2016), with more than 350 microlensing events detected (Wyrzykowski et al. 2023) and over 1700 predicted using astrometric simulations (Klüter et al. 2022). Its importance lies in the fact that most of the observed microlensing events occur in the Galactic disk, where the duration of the event is longer such that high order effects can be detected.
Several events have been studied to date with interesting results, introduced below. For example, we have the single lens event, Gaia18cbf (Kruszyńska et al. 2022), with a very long timescale

of ∼ 490 days where the photometric data revealed a lens of ∼ 2 $M_\odot$. We can mention also Gaia19bld (Rybicki et al. 2022; Bachelet et al. 2022; Cassan et al. 2022), a high-magnification event with a dark lens of 1.1 $M_\odot$. This type of events happens when the source comes very close to the central caustic (Griest & Safizadeh 1998), which is the set of points where the magnification diverges Gaia has also discovered binary lens events. Most notably is the spectacular event Gaia16aye (Wyrzykowski et al. 2020), one of the first microlensing event detected by Gaia which has such a long time scale (over ∼ 500 days) that it was possible to obtain a full orbital solution for this system.

The most crucial advantage of Gaia observations of microlensing events is the fact that Gaia obtains also astrometric time-series with sub-milliarcsecond precision (Rybicki et al. 2018). Therefore, with the data to be released in Gaia DR4, for many of the sources observed between 2014-2019, it will be possible to obtain the size of the angular Einstein ring radius θ_E thus obtaining mass/distance relation for the lenses, in particular for dark lenses (Dominik & Sahu 2000; Belokurov & Evans 2002; McGill et al. 2018; Klüter et al. 2022; Jabłońska et al. 2022).

The DR3 Gaia data release covered 34 months of observations where every target was observed about 40 times (Gaia Collaboration et al. 2016). With these measurements it was possible to obtain various parameters such as the parallax, the proper motion, and other quantities useful for studying the microlensing event. Difficulties arise when the parallax reported by Gaia corresponds regards a microlensing event where the blend flux (the flux of nearby unresolved objects not affected by microlensing) is very high and mainly generated by the lens. A possible interpretation is that both the source and the lens contribute to the total flux making the parallax measured by Gaia (and also the proper motion) a flux-weighted average of the parallaxes of lens and source. With this assumption it is possible to derive a constraint on the lens parameters which will then be explained in detail. This is what we have done in the study of the microlensing event Gaia21blx which also benefits from follow-up by the OMEGA collaboration. The paper is organized as follows. Section 2 is dedicated to the observations and data reduction. In Section 3 we introduce the modeling of this event that leads to four degenerate solutions. We discuss means to break this degeneracy in Section 4, and we propose a method to single out the most likely physical model after accurate evaluation of the probabilities of possible alternatives and derive the physical parameters of the lens. In Section 5, we discuss the kinematics of lens and source. In the last section, we summarize the results obtained.

2. Observations

Gaia21blx is located in the Galactic Disk at (R.A., decl.) = ($14^h53^m15^s.42$, $-62°01'30''.61$) corresponding to Galactic coordinates l = 316.69911°, b = −2.45443°. The alert was published on 22 March 2021 by Gaia Science Alerts (GSA) system (Hodgkin et al. 2021) with magnitude of ∼ 16.64. The photometric measurements obtained by Gaia consist of a wide G-band (Jordi et al. 2010) performed on a monthly period and publicly available at the GSA. The photometric errors for the 153 measurements used in this work are calculated following the procedure described Kruszyńska et al. (2022).

In response to the Gaia Alert, high cadence follow-up observations were obtained by the OMEGA Project, using the Las Cumbres Observatory Global Telescope Network (LCO) of 1m telescopes (Brown et al. 2013). Data were collected in SDSS-g' and -i' bandpasses using the LCO Sinistro instruments, from LCO sites at the Cerro Tololo Interamerican Observatory, Chile (CTIO), the South African Astronomical Observatory (SAAO), Sutherland, South Africa, and the Siding Spring Observatory in Australia. The instrumental signatures were removed from the resulting image data using LCO's BANZAI pipeline (McCully et al. 2018), after which Difference Image Analysis was used to derive timeseries photometry using the pyDANDIA software package (Bramich 2008; Bramich et al. 2013). The process of calibration of the reference images in the g' and i' bands is explained in Street et al. (2024). In short, the instrumental magnitudes are aligned to the VPHAS (Drew et al. 2014) or the Gaia synthetic photometry (Montegriffo et al. 2023), depending on the availability of the catalog for this part of the sky, after an astrometric crossmatch. The linear relationship obtained is ultimately, as well as the errors, propagated to the entire photometry. The Sinistro instruments on the LCO 1m network are designed to be extremely similar. Their detectors have very similar read noise properties, and the difference between the read-noise of every detectors are negligible in the final photometry. The LCO's BANZAI pipeline also removes the instrument-specific/telescope optics signature, using calibration frames specific to each camera. The image data from different telescopes are only combined after this point, in order to process the instrument-signature-corrected images with the DIA pipeline. Processing all images using a single reference image is advantageous at this stage because DIA inherently computes the time-variable component of the flux, relative to that image (in each bandpass). If the data are separated by instrument, then the lightcurve from each instrument is calculated relative to reference images taken under different atmospheric conditions, meaning that in order to combine the datasets for analysis, a second step of calibrating the photometry between the different reference images is required, introducing an additional source of uncertainty. When the data are combined into a single dataset, this additional step is not required. This procedure has been also adopted in previous works and has become a standard for OMEGA data (Rybicki et al. 2022; Olmschenk et al. 2023).

A fourth dataset is obtained by the MiNDSTEp collaboration (Dominik et al. 2010) using the Danish 1.54 Telescope located at ESO La Silla in Chile. This telescope is equipped with a multiband EMCCD instrument (Skottfelt et al. 2015) and the images used were reduced using PyDandia. In total we collect 153 data points in the Gaia-G band, mostly taken before the event while we have 196 data points in i′ band and 89 data points in g′ band. Following common practice in microlensing (Yee et al. 2012; Miyake et al. 2012), we rescale the error bars following $\sigma_i^2 = k\sqrt{\sigma_{i,\mathrm{orig}}^2 + e_{\mathrm{min}}^2}$ where, in this case, we adopt $e_{\mathrm{min}} = 0.03$ for the LCO telescope in i' band, which covers the peak of the event, and we set $e_{\mathrm{min}} = 0$ for the other telescopes, while k ensures that χ^2/d.o.f.=1 for the best model.

3. Modeling

The microlensing effect can be described by the Einstein angle, which describes the angular scale of the event:

$$\theta_E = \sqrt{\frac{4GM\pi_{\mathrm{rel}}}{c^2}} \tag{1}$$

where G is the gravitational constant, c the vacuum speed of light, M being the total lens mass, and $\pi_{\mathrm{rel}} = \mathrm{au}/D_L - \mathrm{au}/D_S$ the relative source-lens parallax with D_L the lens distance and D_S the source distance. The simplest case of microlensing event, the point source single lens, can be described by three parameters: the time of lens-source closest approach t_0, the impact

Table 1. Data from telescopes with their corresponding rescaling parameters and the limb darkening coefficients as derived from stellar models (see Sect. 4.2)

Telescope	Band	N. data	k	e_{min}	Limb darkening
LCO_{gp}	SDSS-g'	85	1.275	0	0.642
LCO_{ip}	SDSS-i'	223	0.727	0.03	0.415
Danish 1.54m	R	28	2.846	0	0.461
Gaia	G-Gaia	153	1.039	0	0.514

parameter in units of Einstein angle u_0 where the source flux reaches the maximum, the Einstein time $t_E = \theta_E/\mu$ where μ is the relative lens-source proper motion in the geocentric reference frame. In addition to these we can have the finite source effect $\rho_* = \theta_*/\theta_E$ with θ_* the angular radius of the source. The inclusion of a second lens requires the addition of three more parameters: the separation in units of Einstein angle between the two lenses s, the mass ratio q and the angle between the source trajectory and the orthogonally projected separation vector from secondary lens to primary lens α. Based on the values of s and q we can have three different configurations: the close configuration where $s < 1$, the intermediate where $s \sim 1$ and the wide configuration where $s > 1$ (Dominik 1999) With this configuration we have the static binary lens model where we approximate the relative lens-source motion as rectilinear, assuming a short time scale. For long timescales we often need to include high order effects. The first is the annual parallax effect, caused by the motion of the Earth around the Sun. This effect on microlensing lightcurves is quantified by (Gould 2000)

$$\pi_E = \frac{\pi_{rel}}{\theta_E} \tag{2}$$

and depends on the direction of the proper motion in the sky. The parallax vector is defined as $\boldsymbol{\pi}_E = \pi_E \hat{\mu}_{LS}$ (An et al. 2002; Gould 2004) and allows us to analyze this effect using the two parameters $\pi_{E,N}$ and $\pi_{E,E}$ that are its northern and eastern component. Another way to determine the parameters of the system is considering the satellite parallax (Refsdal 1966; Gould & Loeb 1992; Gould et al. 2009). Observing the same event simultaneously from two different locations (Earth and space) they measure a different u_0 and t_0. When we have observations from a satellite a fourfold degeneracy arises, due to the fact that the sign of u_0 cannot be determined. This degeneracy can be broken by measuring orbital motion or, if that is not detectable, reduced to a twofold degeneracy that can be broken with the Rich Argument (Calchi Novati et al. 2015). The second effect is the orbital motion of the two lenses around their common center of mass. In principle it would be preferable to use the full Keplerian orbit parametrization (Skowron et al. 2011). Of course, there is no reason a priori to assume zero eccentricity for a stellar binary system. However, the introduction of too many unconstrained parameters would complicate the fit without any benefits. A minimal fit for orbital motion is typically made considering two components but this leads to unphysical orbital trajectories (Bozza et al. 2021). We prefer to opt for a fit including the three components of the angular velocity of the system assuming a circular orbit (Skowron et al. 2011; Bozza et al. 2021), so as to explore physical orbital trajectories. We will see that even these additional parameters are poorly constrained, making a full Keplerian fit superfluous. We then describe the orbital motion with the following parameters: the parallel component of the projected angular velocity parallel to the lens axis at time t_0, $\gamma_\parallel = (ds/dt)/s$, the perpendicular component $\gamma_\perp = -(d\alpha/dt)$ and the component of the angular velocity along the line of sight $\gamma_z = (ds_z/dt)/s$ where s_z is the separation in units of Einstein radius between the two lenses along the line of sight.

The parameters presented above are necessary to describe a model flux $F(t)$ of the magnified source as a function of time:

$$F(t) = A(t)F_S + F_b \tag{3}$$

where $A(t)$ is the magnification of the source flux as a function of time, F_S is the baseline of the source flux and F_b is the blend flux, or the flux not affected by microlensing.

To explore the parameter space, we use the RTModel platform [1] based on VBBinaryLensing codes (Bozza 2010; Bozza et al. 2018, 2021). RTModel makes a full exploration of all corners of the parameter space of binary lensing thanks to a complete library of templates (Mao & Di Stefano 1995; Liebig et al. 2015) covering all possible classes of light curves arising from different caustic topologies and different trajectories of the source. RTModel returns two main models: a close binary and a wide binary model, whose parameters are shown in Table 2, with the source trajectory orthogonal to the binary lens axis and crossing the cusp of the central caustic between the two lenses. In both cases, we find a significant improvement of the fit if we include the annual parallax. In this case, the reflection symmetry around the lens axis is broken and we must distinguish models with positive and negative u_0, which would be equivalent in the static binary case (see Table 3). We label the four models as C+, C-, W+, W-, where C or W distinguish close and wide binary respectively and the sign refers to the sign of the impact parameter u_0. In addition to parallax, we also check for orbital motion obtaining a modest improvement. Nevertheless, the inclusion of orbital motion has an impact on the error bars of the parallax components and should therefore be considered even if the orbital motion remains poorly constrained. The physical consequences of orbital motion are therefore not considered, as the parameters are not robustly determined. From the best solution obtained with RTModel we run Markov Chains to make a complete exploration of the local χ^2 minima to get full information about the uncertainties and the correlations in the parameters. We consider also the possibility to have a binary source single lens system but this gave a $\chi^2 \approx 730$, very far from the chi-square values obtained by the best models ($\Delta\chi^2 \approx 250$). We therefore excluded this configuration from the analysis.

In Figure 1 we show the C+ model (the zoom of the peak is shown in Fig. 2), the other models are indistinguishable. All the caustic configurations and the source trajectories are shown in Fig. 3. The final parameters, including the orbital motion, are shown in Table 4. We can easily note that the χ^2 values are similar, which forces us, at first, to retain all competitive models.

4. Constraints on the lens

From the four models we derive the source flux and the blend flux listed in Table 5. We can immediately note that the blend is very high for all the models. The blend can have multiple

[1] https://www.fisica.unisa.it/GravitationAstrophysics/RTModel.htm

Table 2. Parameters of the two binary lens models obtained with RTModel after a Markov Chain. The parameters are obtained combining ground data and Gaia data.

Parameters	(Unit)	Close	Wide
t_E	days	$167.4^{+17.7}_{-3.2}$	$79.2^{+2.4}_{-1.2}$
t_0	HJD-2450000	$9299.05^{+0.21}_{-0.07}$	$9299.34^{+0.20}_{-0.20}$
u_0		$0.0560^{+0.0022}_{-0.0035}$	$0.1062^{+0.0175}_{-0.0175}$
ρ_*	10^{-3}	$1.69^{+0.05}_{-0.19}$	$3.52^{+0.16}_{-0.13}$
α		$-4.809^{+0.007}_{-0.020}$	$-4.856^{+0.003}_{-0.004}$
s		$0.364^{+0.003}_{-0.014}$	$1.867^{+0.017}_{0.017}$
q		$0.876^{+0.049}_{-0.146}$	$0.176^{+0.009}_{-0.009}$
χ^2		598.3	657.5

Table 3. Parameters of the four cases of binary lensing model with parallax obtained from the modeling of the lightcurves using the Markov Chain. The parameters are obtained combining ground data and Gaia data.

Parameters	(Unit)	C+	C-	W+	W-
t_E	days	$124.4^{+9.9}_{-4.4}$	$120.0^{+11.0}_{12.0}$	$90.7^{+6.4}_{-7.6}$	$97.2^{+3.4}_{-2.2}$
t_0	HJD-2450000	$9301.31^{+0.39}_{-0.30}$	$9300.70^{+0.29}_{-0.24}$	$9297.34^{+0.08}_{-0.27}$	$9297.73^{+0.31}_{-0.31}$
u_0		$0.1003^{+0.0052}_{-0.0081}$	$-0.0954^{+0.0086}_{-0.0065}$	$0.0365^{+0.0100}_{-0.0034}$	$-0.0175^{+0.0137}_{-0.0137}$
ρ_*	10^{-3}	$2.28^{+0.10}_{-0.19}$	$2.38^{+0.26}_{-0.26}$	$3.12^{+0.28}_{-0.24}$	$2.86^{+0.13}_{-0.12}$
α		$-4.958^{+0.018}_{-0.022}$	$4.930^{+0.016}_{-0.016}$	$4.948^{+0.010}_{-0.038}$	$-4.956^{+0.022}_{-0.011}$
s		$0.468^{+0.013}_{-0.020}$	$0.456^{+0.016}_{-0.021}$	$2.018^{+0.011}_{-0.004}$	$1.998^{+0.015}_{-0.015}$
q		$0.505^{+0.030}_{-0.058}$	$0.575^{+0.035}_{-0.044}$	$0.255^{+0.010}_{-0.010}$	$0.223^{+0.016}_{-0.001}$
$\pi_{E,N}$		$0.187^{+0.018}_{-0.039}$	$0.102^{+0.030}_{-0.033}$	$0.133^{+0.054}_{-0.101}$	$0.134^{+0.032}_{-0.019}$
$\pi_{E,E}$		$-0.077^{+0.024}_{-0.023}$	$-0.191^{+0.037}_{-0.024}$	$-0.270^{+0.030}_{-0.021}$	$-0.164^{+0.032}_{-0.014}$
χ^2		485.5	487.0	486.0	487.0

Table 4. Parameters of the four models from the modeling of the lightcurves using the Markov Chain. The parameters are obtained combining ground data and Gaia data.

Parameters	(Unit)	C+	C-	W+	W-
t_E	days	$148.3^{+8.7}_{-7.0}$	$134.1^{+18.9}_{-14.1}$	$103.0^{+6.8}_{-7.3}$	$116.7^{+10.3}_{-18.7}$
t_0	HJD-2450000	$9300.29^{+0.20}_{-0.51}$	$9299.66^{+0.16}_{-0.34}$	$9297.38^{+0.07}_{-0.35}$	$9297.96^{+0.08}_{-0.08}$
u_0		$0.0888^{+0.0017}_{-0.0064}$	$-0.1032^{+0.0127}_{-0.0072}$	$0.0323^{+0.0030}_{-0.0030}$	$-0.0070^{+0.0027}_{-0.0006}$
ρ_*	10^{-3}	$1.86^{+0.15}_{-0.14}$	$2.13^{+0.24}_{-0.30}$	$2.67^{+0.23}_{-0.21}$	$2.41^{+0.21}_{-0.36}$
α		$-4.875^{+0.022}_{-0.018}$	$4.830^{+0.007}_{-0.031}$	$4.970^{+0.014}_{-0.003}$	$-5.030^{+0.080}_{-0.050}$
s		$0.432^{+0.006}_{-0.014}$	$0.464^{+0.017}_{-0.029}$	$2.013^{+0.010}_{-0.001}$	$1.989^{+0.027}_{-0.027}$
q		$0.555^{+0.067}_{-0.043}$	$0.491^{+0.023}_{-0.078}$	$0.233^{+0.013}_{-0.009}$	$0.210^{+0.017}_{-0.016}$
$\pi_{E,N}$		$0.134^{+0.018}_{-0.033}$	$0.088^{+0.056}_{-0.007}$	$0.233^{+0.022}_{-0.059}$	$0.185^{+0.028}_{-0.062}$
$\pi_{E,E}$		$0.018^{+0.014}_{-0.035}$	$-0.073^{+0.034}_{-0.038}$	$-0.202^{+0.024}_{-0.031}$	$-0.118^{+0.035}_{-0.065}$
$\gamma_\parallel$	year^{-1}	$-1.32^{+0.47}_{-0.15}$	$-1.76^{+0.66}_{-0.44}$	$0.10^{+0.33}_{-0.07}$	$0.12^{+0.47}_{-0.44}$
$\gamma_\perp$	year^{-1}	$-0.16^{+0.29}_{-0.33}$	$1.77^{+0.58}_{-0.11}$	$-0.15^{+0.22}_{-0.07}$	$1.34^{+0.66}_{-1.02}$
γ_z	year^{-1}	< 1.92	< 2.53	< 1.11	< 2.65
χ^2		477.0	477.9	482.5	485.7

Table 5. Magnitudes of baseline and blend, indicated with the subscript S and b respectively, of the four models for each telescope.

	Unit	C+	C-	W+	W-
G_S	mag	19.557 ± 0.062	19.367 ± 0.137	18.375 ± 0.079	18.476 ± 0.128
G_b	mag	18.200 ± 0.018	18.261 ± 0.049	19.101 ± 0.155	18.927 ± 0.193
g_S	mag	21.284 ± 0.065	21.107 ± 0.143	20.113 ± 0.073	20.212 ± 0.135
g_b	mag	19.225 ± 0.010	19.256 ± 0.027	19.597 ± 0.045	19.542 ± 0.073
i_S	mag	19.147 ± 0.062	18.972 ± 0.145	17.975 ± 0.070	18.074 ± 0.132
i_b	mag	17.362 ± 0.090	17.401 ± 0.034	17.870 ± 0.063	17.780 ± 0.102

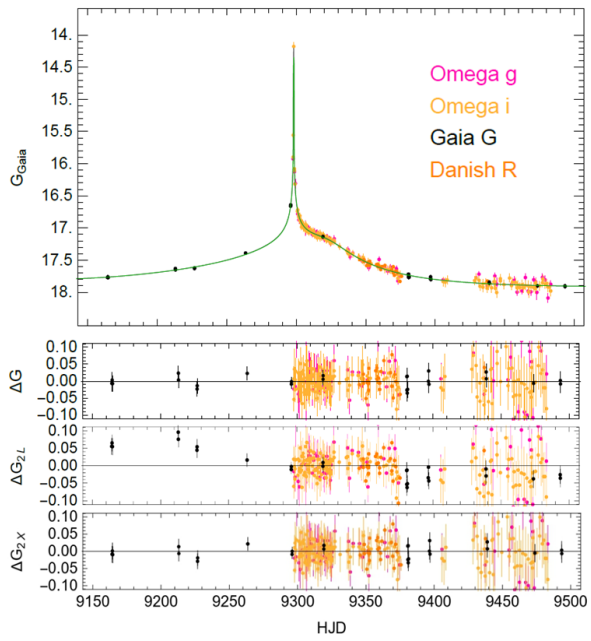

Fig. 1. Lightcurve with residuals of the best model, C+, for the microlensing event Gaia21blx. Below the residuals of the best model we include also the residuals for the static configuration (labeled 2L) and the binary lensing model with only parallax and no orbital motion (labeled 2X).

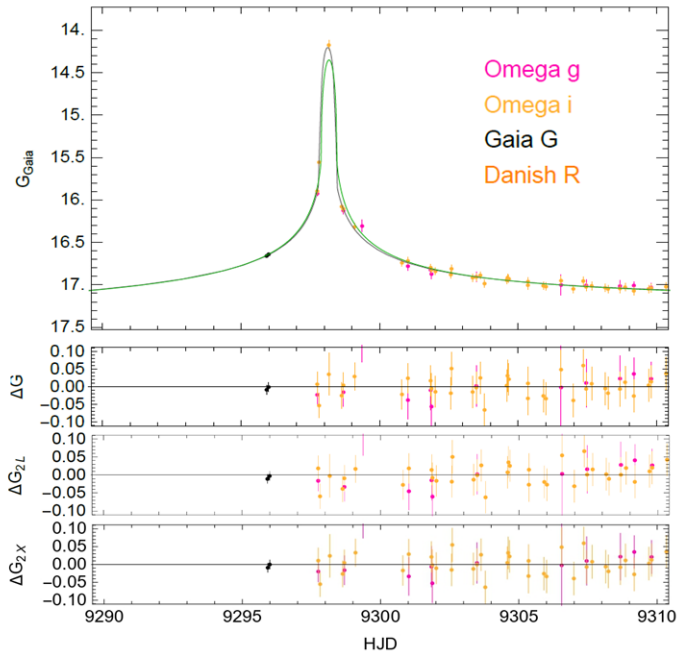

Fig. 2. Zoom of the lightcurve with residuals of the best model, C+, at the peak. The grey lightcurve is the microlensing light curve as seen from Earth, while the green line is the light curve as seen from Gaia. Below the residuals of the best model we include also the residuals for the static configuration (labeled 2L) and the binary lensing model with only parallax and no orbital motion (labeled 2X).

origins: it may come from very close field stars, from a second source that is not affected by microlensing, from the lens itself or from a combination of these cases. In this context, being the lens a binary system formed by two stars, it is plausible that its flux makes some contribution to the blend or even explain it

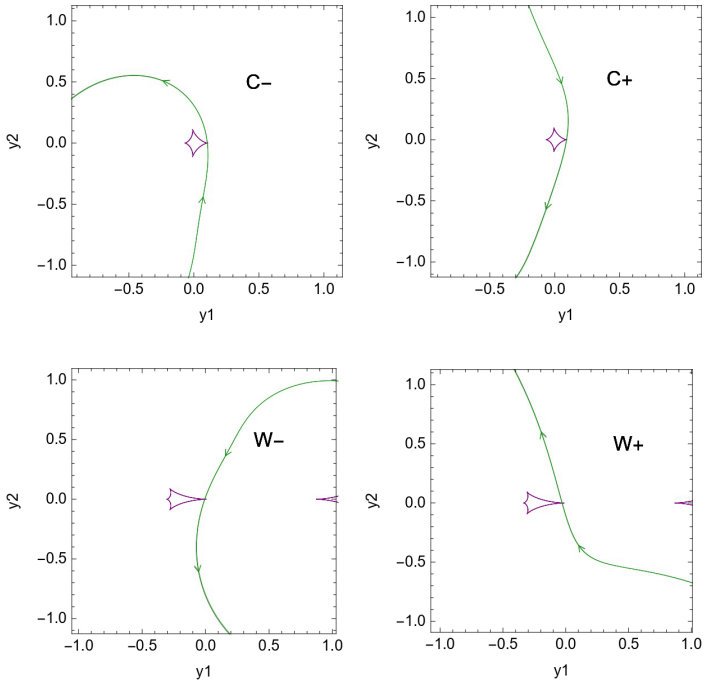

Fig. 3. Caustic configuration (in purple) for all the models with the source trajectories (the green lines with arrows). On the top we have the C- on the left while on the right there is the C+. On the bottom on the left we have the W- model and then on the right the W+ model. Coordinates are centered with respect to the center of mass of the two lenses and are in unit of θ_E

totally. In the case of a partial contribution only, we should invoke a second source or a field star to explain the residual blend flux. Although this is still possible, considering that Gaia21blx is a disk event where there is a lower stellar density than the bulge, the chance alignment of a third object seems relatively unlikely. Therefore, we start with the simplest assumption that the blend is totally caused by the binary lens itself, thus dealing with the minimal number of objects needed to explain the observations, and check that the results are fully sound from all physical points of view. Only if we find any inconsistencies we would be pushed to consider a more complicated system with a third system aligned along the same line of sight. We then use the parallax measured by Gaia derived from the Gaia-DR3 release $\pi_{\rm Gaia} = (0.45 \pm 0.13)$ mas with a Re-normalized Unit Weight Error (RUWE) of 1.18. A RUWE with this value means that the parallax measured by Gaia is reliable, had it been higher than 1.4 it would have indicated the presence of systematics (Lindegren 2018; Bachelet et al. 2022).

At this point we assume that the Gaia parallax does not correspond to the source or lens parallax only but rather the flux-weighted average of the parallaxes of lens and source. Introducing the lens parallax $\pi_{\rm L}$ and the source parallax $\pi_{\rm S}$ we relate these two quantities with $\pi_{\rm Gaia}$ using the following equation:

$$\pi_{\rm Gaia} = \frac{\pi_{\rm S}\, 10^{-0.4\, G_S} + \pi_{\rm L}\, 10^{-0.4\, G_L}}{10^{-0.4\, G_S} + 10^{-0.4\, G_L}}\,, \tag{4}$$

where $G_{\rm L} = G_{\rm b}$. From now on, we will use this equation to replace π_S as a function of π_L.

4.1. Blend flux constraint

With the assumption made in Eq.4 we have the combined information on lens and source and restrict the physical range of the parameters which will be useful to explore the region in the $D_{\rm L}$–M space where the lens lies. A first way to explore this region is using a mass-luminosity relation (MLR). Since there are no MLR in the Gaia band for low-mass stars (Malkov et al. (2022) provide a MLR but stopped at 1.4 $M_\odot$) we must convert the magnitudes in V-band where MLR for low-mass stars are available. To this purpose, we use the relation in Riello et al. (2021) and we derive the Gaia color $G_{\rm BP} - G_{\rm RP}$ from the color $g' - i'$ with

$$\begin{aligned} G_{\rm BP} - G_{\rm RP} &= 0.3971 + 0.777\,(g' - i') - 0.4164\,(g' - i')^2 + \\ &\quad + 0.008237\,(g' - i')^3\,. \end{aligned} \tag{5}$$

Once we obtain the Gaia color from Eq. (5), we take the equation that relates the G-Gaia band with Johnson V-band using the Gaia color in order to obtain the V magnitude for the lens,

$$\begin{aligned} G - V &= -0.02704 + 0.01424\,(G_{\rm BP} - G_{\rm RP}) - \\ &\quad - 0.2156\,(G_{\rm BP} - G_{\rm RP})^2 + \\ &\quad + 0.01426\,(G_{\rm BP} - G_{\rm RP})^3\,. \end{aligned} \tag{6}$$

Including the extinction along the line of sight following the work of Capitanio et al. (2017) we use the apparent magnitude obtained to write the equation for the absolute magnitude

$$M_{\rm V,L}(M) = V_{\rm L} - 5\log(D_{\rm L}) - A_{\rm V}(D_{\rm L})\,, \tag{7}$$

where the dependence on the lens distance is made explicit.

At this point we use the MLR of Xia et al. (2008). Since the lens is binary, we consider the two components separately using

$$\log M_i = \begin{cases} 0.213 - 0.0250\,M_{{\rm V},i} - 0.00275\,M_{{\rm V},i}^2 \\ \qquad \text{for} \quad M_i \in (0.50, 1.086)\,M_\odot \\ 0.982 - 0.128\,M_{{\rm V},i} \\ \qquad \text{for} \quad M_i \in [0.28, 0.50]\,M_\odot \\ 4.77 - 0.714\,M_{{\rm V},i} + 0.0224\,M_{{\rm V},i}^2 \\ \qquad \text{for} \quad M_i \in (0.1, 0.28)\,M_\odot \end{cases} \tag{8}$$

and in the end sum over the fluxes of the two lenses.

The mass ratio q is fixed by the microlensing modeling, while the total mass will be obtained requiring that the total magnitude of the system $M_{\rm V}$ matches $M_{\rm V,L}$ as derived from Eq. 7. In this way we derive the mass as a function of the distance.

4.2. Finite source effect constraint

From the source angular size we get another constraint: following Boyajian et al. (2014) we derive θ_* using the color $g' - i'$ to derive the zero-magnitude angular diameter $\theta_{m_\lambda=0}$, that represents the angular diameter of a star when it is at a distance at which its apparent magnitude equals zero expressed by the polynomial (Boyajian et al. 2014)

$$\log\theta_{m_{g'}=0} = 0.692 + 0.543\,(g' - i') - 0.021\,(g' - i')^2 \tag{9}$$

The source angular diameter is obtained as (Boyajian et al. 2014; Barnes et al. 1978)

$$\log\,\theta_* = \log\,\theta_{m_\lambda=0} - 0.2\,m_\lambda\,, \tag{10}$$

where m_λ is the apparent magnitude of a star in a certain filter λ. In this case we use the value of $g'_{\rm S}$ for our source as found in Table 5 .
In this way, having both θ_* and ρ_* we are able to derive θ_E, since that $\theta_E = \theta_*/\rho_*$. The Einstein angle combined with the Gaia parallax (remembering that π_S is obtained by Eq. 4), gives us another relation between mass and distance explained as

$$M = \frac{\theta_{\rm E}^2}{\kappa\,(\pi_{\rm L} - \pi_{\rm S})}\,. \tag{11}$$

4.3. Microlensing parallax constraint

We can get a third constraint using the microlensing parameters, in particular, the parallax obtained from the Markov Chain π_E that combined with Gaia parallax gives us

$$M = \frac{\pi_{\rm L} - \pi_{\rm S}}{\kappa\,\pi_{\rm E}^2}\,. \tag{12}$$

4.4. Combination of the three constraints

The three constraints appear as three colored bands whose widths track the uncertainties at 1 σ as shown in Fig. 4. We can note that the parallax error is 30% making it the weakest constraint. The most restrictive bound comes from the MLR, while the constraint of finite source effects becomes an upper bound for the lens distance when D_L and D_S tend to coincide. We have a compatible solution if there is overlap between all three allowed regions. This happens for both close cases, C+ and C-, while the wide case W- is slightly disfavored, since there is only a small overlap region within the allowed stripes at 1 σ. The W+ is instead excluded at over 5 σ. We also note that the wide models are also slightly disfavored by the χ^2 as evident in Table 4. In Table 6 we report the allowed range for mass and lens distance by identifying the region where the three constraints overlap for the best model C+. The C- model gives us similar result with a $D_{\rm L} = 2.17 \pm 0.06$ kpc and $M = 1.41 \pm 0.15\,M_\odot$ composed by two lenses of $M_1 = 0.94 \pm 0.15\,M_\odot$ and $M_2 = 0.46 \pm 0.06\,M_\odot$ respectively. The small overlap region for the W- model corresponds to a binary lens of $\sim 0.9\,M_\odot$ distant ~ 1.8 kpc composed by a K star and a M dwarf (see Table 7. From the combination of the three constraints we are also able to calculate the Einstein angle $\theta_E = 0.69 \pm 0.50$ mas and the projected separation $a_\perp = 0.65 \pm 0.47\,au$. For the W- model we have $\theta_E = 1.16 \pm 0.10$ mas and $a_\perp = 4.15 \pm 0.36\,au$

A further consistency check of our assumption on Gaia parallax is given by astrometry. Using the latest version of VBBinaryLensing of Bozza et al. (2021) we are able to simulate the astrometric microlensing of the event as shown in Fig. 5. The fact that the baseline of Gaia data is very long compared to the microlensing duration and the absence of Gaia points during the magnified section of the lightcurve strengthens the hypothesis that the parallax measured by Gaia is largely unaffected by microlensing and that can be considered the flux-weighted average of the parallaxes of lens and source.

Using IAC-STAR (Aparicio & Gallart 2004) with the stellar evolution library of Girardi et al. (2000) we extrapolate the magnitude in the Johnson Cousin's bands. In this way using the conversion from Johnson to SDSS band Davenport et al. (2006) we are able to obtain the g' and i' band for each lens and using the formulas present in Riello et al. (2021) backwards, the

Table 6. Physical parameters of lens and source for the best model C+

	Distance (kpc)	Mass ($M_\odot$)	g'	i'	G (Gaia)	Spectral class
Total lens	2.18 ± 0.07	1.48 ± 0.17	19.225 ± 0.010	17.362 ± 0.090	18.200 ± 0.018	-
Primary lens	2.18 ± 0.07	0.95 ± 0.12	20.023 ± 0.530	17.697 ± 0.530	18.016 ± 0.749	G star
Secondary lens	2.18 ± 0.07	0.53 ± 0.07	25.000 ± 0.514	20.601 ± 0.514	20.411 ± 0.727	K star
Source	2.38 ± 0.31	1.10 ± 0.18	21.284 ± 0.065	19.147 ± 0.062	19.557 ± 0.062	Subgiant F star

Table 7. Physical parameters of lens and source for the alternative model W-

	Distance (kpc)	Mass ($M_\odot$)	g'	i'	G (Gaia)	Spectral class
Total lens	1.79 ± 0.07	0.94 ± 0.09	19.542 ± 0.073	17.780 ± 0.102	18.927 ± 0.193	-
Primary lens	1.79 ± 0.07	0.78 ± 0.08	21.312 ± 0.653	18.306 ± 0.653	18.469 ± 0.924	K star
Secondary lens	1.79 ± 0.07	0.16 ± 0.02	29.551 ± 0.675	24.401 ± 0.675	24.575 ± 0.954	M star
Source	2.63 ± 0.10	0.96 ± 0.09	20.212 ± 0.135	18.074 ± 0.132	18.476 ± 0.128	G star

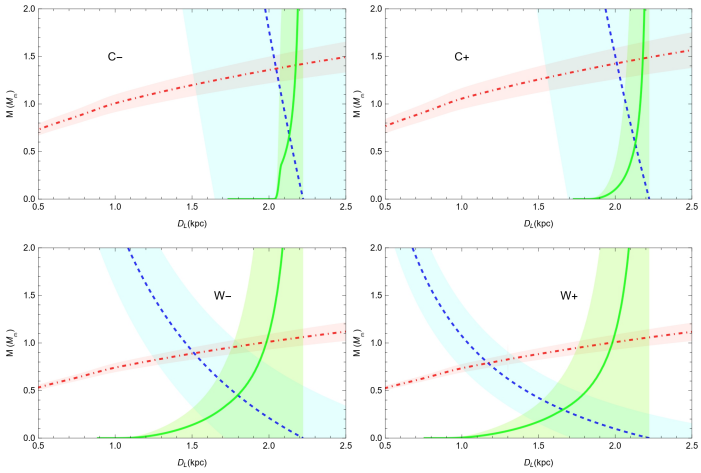

Fig. 4. M–D_L region for all the models. The blue stripe with the dashed line represents the M–D_L relation obtained by microlensing parallax (π_E). The red stripe with the dot-dashed line shows the constraint from the lens flux where mass-luminosity relations for low-mass stars are used. The green stripe with the continuous line exhibits the constraint obtained from the finite source effects (Boyajian et al. 2014) and the angular radius of the source. All the stripes have a range of 1σ

magnitude is also obtained in the Gaia band, as reported in Table 6. Concerning the source we can conclude that is about 2.4 kpc distant and probably an F subgiant star. Both lens and source are located between the Sagittarius arm and the Centaurus arm (see Fig. 6). For the wide solution we obtain a G star source located in the Centaurus arm at 2.6 kpc from the Sun.

4.5. Limb Darkening

We have included the limb darkening of the source brightness profile in our models, since the finite source effects play a significant role. To ensure accurate estimation of the linear limb-darkening coefficients for each telescope, we proceeded as follows: using IAC-Star (Aparicio & Gallart 2004) with the stellar evolution library of Girardi et al. (2000) we started from the absolute magnitude in V band obtained for the source and we simulated a stellar population with the solar metallicity from which we obtain $\log g = 4.2^{+0.3}_{-0.2}$ and $T_{\rm eff} = 6100^{+400}_{-350}$ K. Using these values we derived the linear limb-darkening coefficients from van Hamme (1993) for each telescope listed in Table 1. The limb darkening does not affect the final result, as we explicitly verified by repeating the analysis with the values at the extremes of the intervals. This is reinforced by the fact that there are not enough points on the peak to be sensitive to such fine details.

4.6. Possible source contaminations

The assumption that the blending flux is generated entirely by the lens does not mean that it is the only plausible hypothesis. Here we attempt to quantify the probabilities for alternative explanations of the blending flux. Firstly, we consider the hypothesis that there is a third object that is not associated with either the lens or the source, and is therefore a field star that affects the blend flux at least more than 10%. Using the latest updated version of the Besançon model (Lagarde et al. 2017, 2019), we simulate a stellar population in the vicinity of the target, covering an area of 0.2 square degrees. Taking into account that the minimum separation detectable by Gaia is 0.05 square arcseconds (de Bruijne et al. 2015), we calculate the probability of a random alignment of a third object, which turns out to be 0.001%. The hypothesis that there is a third object is therefore very unlikely, but in this case, the blending flux would be an upper limit on the flux of the lens and hence on the mass. Considering both the best models obtained from microlensing and the fact that the RUWE obtained from GaiaDR3 is 1.14, we can exclude the presence of a third lens or a nearby secondary source. Regarding the possibility that the contaminant is a very wide companion of the source and considering that for F, G, K type stars, the probability that they are part of binary or multiple systems is 46% (Raghavan et al. 2010). Given the previously calculated $\theta_E = 0.69 \pm 0.50$ mas, in order for the source to have a companion that is not detected by Gaia and that does not shows up in the microlensing light curve, it must be in a region that extends from Gaia's minimum resolution of 230 mas and $1/4\theta_E = 0.36$ mas. Following the work of Fukui et al. (2015) we calculate the probability to have a companion source in this range. Firstly, using Gaia's minimum resolution and the maximum angular distance detectable by microlensing, and always assuming a source distance of 2.38 kpc, we obtain a separation range between the two companions of 1-550 au. From the Besançon model, always considering a contribution of the secondary source to the blend flux of 10%, we obtain a mass of the latter equal to $0.70 M_\odot$. Applying Kepler's third law, we obtain the period range of this hypothetical binary system, which must be $2.3 < Log(P) < 6.5$. From this, considering the probability of having only a binary or multiple system from Raghavan et al. (2010) of 46%, and using, as always from this work, the period log-normal distribution with mean $P = 5.03$ and standard deviation $\sigma_{logP} = 2.28$, we derive the fraction of binaries in the range of periods calculated earlier,

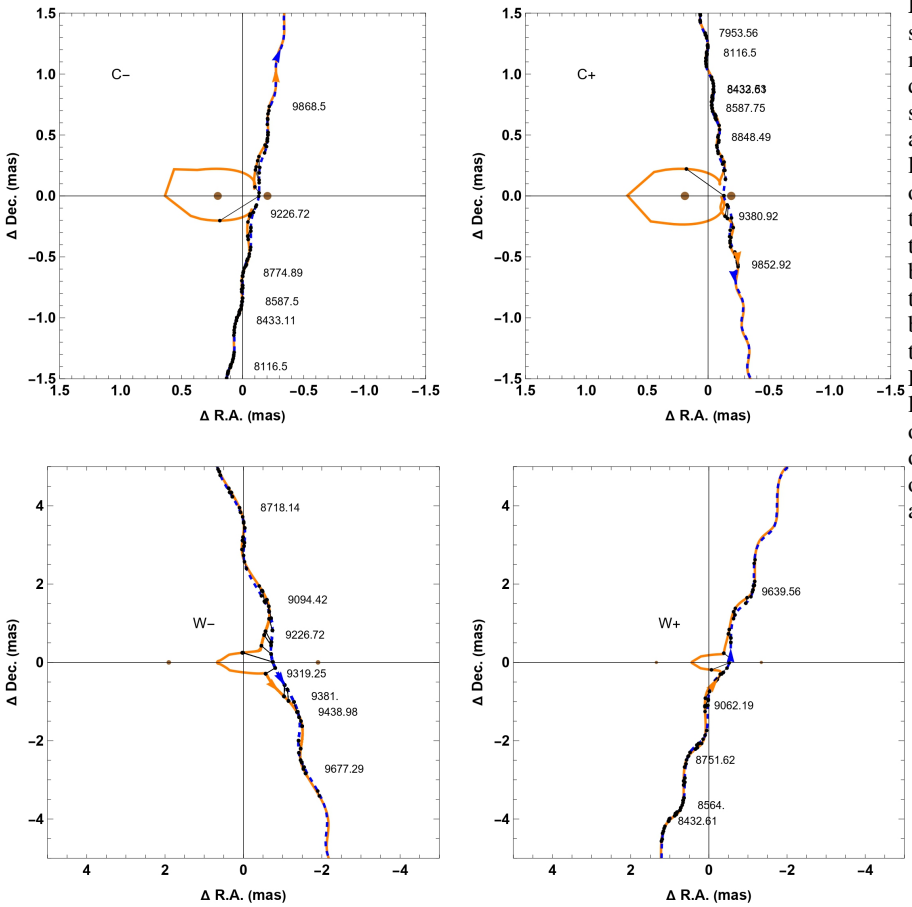

Fig. 5. Astrometry simulation for all the models. The blue dashed curve is the source trajectory in a frame in which the lenses are fixed. The orange curve shows the photo-centroid trajectory. The two brown disks are the two lenses and the black points represent the Gaia data points. For all the models the lens flux considered is obtained by the overlap of the two constraints of finite source effects and blend flux.

which is 62%. Finally, considering the 46% probability of having a binary or multiple system for F-G-K stars, we get a total probability of 28%. Following the same procedure, we can calculate the probability of a third lens acting as a blending lens that has no effect on microlensing, otherwise there would have been further peaks in the light curve. Always considering a contribution of 10% of the total blending flux, following the same approach as for a hypothetical second source, we obtain that the probability of having a third lens is 9%. We repeat the same approach for the wide models and we calculate the probability of having a secondary source not affected by microlensing equal to 30%. About the probability to have a third star in the lens system we get the value of 10 %.

We conclude that all three alternative hypotheses are mildly or strongly disfavored, with the most competitive alternative to our proposed interpretation being a companion to the source. Possible observations to check the correctness of our main conclusion or one of the enumerated alternatives may include high-resolution spectroscopic studies that may confirm the presence of one source and two lenses as described in our model. The relative proper motion is quite small (see Sect. 5), which discourages high-resolution imaging for the separation of lens and source.

5. Lens and source kinematics

Since we have a precise determination of the lens mass and distance both according to model C+ and to model W-, we are in the position of a full description of the kinematics of the lens and source systems. We will describe all details for model C+ and quote the results for W- at the end of the section. For model C+, the relative lens-source proper motion in the geocentric reference frame is

$$\mu_{\rm rel} = \frac{\kappa\, M\, \pi_{\rm E}}{t_{\rm E}} = (1.69 \pm 1.22)\ {\rm mas/yr}\,. \tag{13}$$

Using the eastern and northern components of the parallax vector we can obtain the components of the proper motion in the geocentric frame as

$$\begin{aligned}\boldsymbol{\mu}_{\rm rel,geo} &= \frac{\mu_{\rm rel}}{\pi_{\rm E}}\,(\pi_{\rm E,E}\,\hat{\boldsymbol{E}} + \pi_{\rm E,N}\,\hat{\boldsymbol{N}}) \\ &= [(0.23 \pm 0.85)\,\hat{\boldsymbol{E}} + (1.67 \pm 0.88)\,\hat{\boldsymbol{N}}]\ {\rm mas/yr}\,,\end{aligned} \tag{14}$$

where $\hat{\boldsymbol{E}}$ and $\hat{\boldsymbol{N}}$ are the unit vectors in the plane orthogonal to the line of sight: $\hat{\boldsymbol{N}}$ is tangent to the celestial meridian pointing to the north while $\hat{\boldsymbol{E}}$ is tangent to the celestial parallel pointing to the east direction. It is simple to convert them to the heliocentric reference frame by utilizing the velocity vectors of the Earth at time t_0 projected orthogonally to the line of sight

$$\begin{aligned}\boldsymbol{\mu}_{\rm rel,hel} &= \boldsymbol{\mu}_{\rm rel,geo} + \boldsymbol{v}_{\oplus}\,\frac{\pi_{\rm rel}}{\rm au} \\ &= [(0.41 \pm 0.19)\,\hat{\boldsymbol{E}} + (1.75 \pm 0.12)\,\hat{\boldsymbol{N}}]\ {\rm mas/yr}\,.\end{aligned} \tag{15}$$

Gaia DR3 release also reports proper motion components for Gaia21blx (Riello et al. 2021). As we did for the parallax (see Eq.4), we consider the proper motion measured by Gaia as the flux-weighted average of the lens and source proper motions

$$\begin{aligned}\boldsymbol{\mu}_{\rm Gaia} &= \frac{\boldsymbol{\mu}_{\rm S}\,10^{-0.4\,G_{\rm S}} + \boldsymbol{\mu}_{\rm L}\,10^{-0.4\,G_{\rm L}}}{10^{-0.4\,G_{\rm S}} + 10^{-0.4\,G_{\rm L}}} \\ &= [(-6.81 \pm 0.11)\,\hat{\boldsymbol{E}} + (-3.24 \pm 0.12)\,\hat{\boldsymbol{N}}]\ {\rm mas/yr}\end{aligned} \tag{16}$$

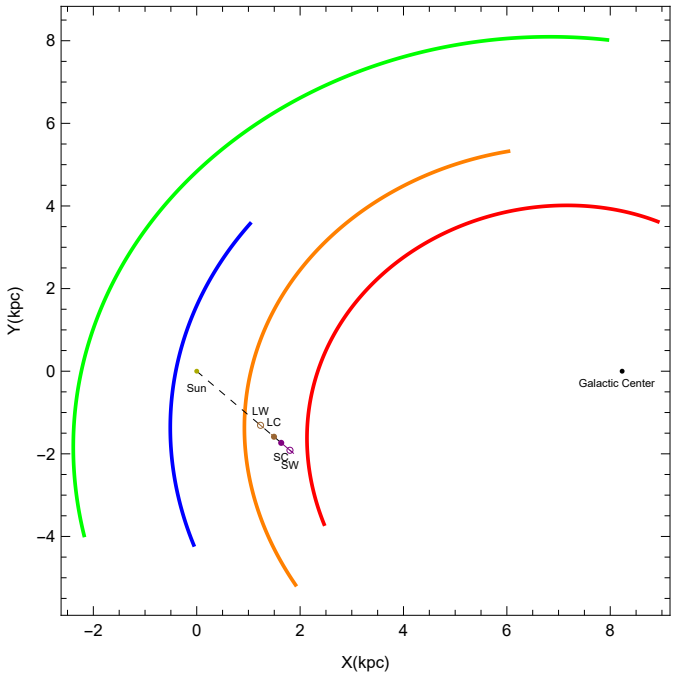

Fig. 6. Configuration of Gaia21blx in the Milky Way. The colored spirals represent (from left to right) the Perseus arm (green), the Local arm (blue), the Sagittarius arm (orange) and the Centaurus arm (Red). In the figure, the Galactic center is represented by the black disk, while the lens and source for the C+ model are represented by the brown and purple disks, respectively. For the W- model, empty circles have been used (same colors as in the previous case). The Sun is the darker yellow point. X and Y are the cartesian coordinates in the Galactic plane, centered at the Sun, with the X axis positive toward the Galactic center and the Y axes directed along the rotational curve. The configuration is computed following the work of Castro-Ginard et al. (2021).

Noting that the relative proper motion is simply the difference between lens and source proper motions ($\boldsymbol{\mu}_{\rm rel,hel} \equiv \boldsymbol{\mu}_{\rm L} - \boldsymbol{\mu}_{\rm S}$), Eqs. (15) and (16) represent two independent linear constraints for $\boldsymbol{\mu}_{\rm L}$ and $\boldsymbol{\mu}_{\rm S}$ which can be easily solved to obtain

$$\begin{aligned}\boldsymbol{\mu}_{\rm L} &= [(-6.73 \pm 0.48)\,\hat{\boldsymbol{E}} + (-2.87 \pm 0.08)\,\hat{\boldsymbol{N}}]\ \mathrm{mas/yr}\,,\\ \boldsymbol{\mu}_{\rm S} &= [(-7.14 \pm 0.48)\,\hat{\boldsymbol{E}} + (-4.55 \pm 0.08)\,\hat{\boldsymbol{N}}]\ \mathrm{mas/yr}\,. \end{aligned} \tag{17}$$

We then apply a 26.84° rotation to these vectors to determine their components in relation to the Galactic frame as

$$\begin{aligned}\boldsymbol{\mu}_{\rm L} &= [(-7.30 \pm 0.48)\,\hat{\boldsymbol{l}} + (0.48 \pm 0.08)\,\hat{\boldsymbol{b}}]\ \mathrm{mas/yr}\,,\\ \boldsymbol{\mu}_{\rm S} &= [(-8.42 \pm 0.48)\,\hat{\boldsymbol{l}} + (-0.84 \pm 0.08)\,\hat{\boldsymbol{b}}]\ \mathrm{mas/yr}\,, \end{aligned} \tag{18}$$

where we have introduced unit vectors pointing in the direction of increasing Galactic longitude $\hat{\boldsymbol{l}}$ and increasing Galactic latitude $\hat{\boldsymbol{b}}$.
Since we know the distances D_L and D_S we can switch from the proper motion to the heliocentric velocity components

$$\begin{aligned}\boldsymbol{v}_{\rm L,hel} &= [(-69.35\pm, 4.96)\,\hat{\boldsymbol{l}} + (-29.68 \pm 0.81)\,\hat{\boldsymbol{b}}]\ \mathrm{km/s}\,,\\ \boldsymbol{v}_{\rm S,hel} &= [(-80.62 \pm 5.41)\,\hat{\boldsymbol{l}} + (-51.35 \pm 0.89)\,\hat{\boldsymbol{b}}]\ \mathrm{km/s}\,. \end{aligned} \tag{19}$$

It is interesting to calculate the peculiar velocities of lens and source with respect to their local standard of rest in order to assign these objects to definite kinematic components of the Galaxy. In order to do that, we must convert the heliocentric velocities to Galactocentric velocities and then subtract the average rotation of the disk at the position of lens and source. Of course, we cannot make a full 3-d reconstruction of the peculiar motion, since we miss the radial velocities of lens and source. However, as long as we just have to add or subtract vectors, we have all the information needed to calculate the components along the directions $\hat{\boldsymbol{l}}$ and $\hat{\boldsymbol{b}}$ orthogonal to the line of sight, which already contain sufficiently interesting information, as we shall see in a while.

The Galactocentric velocities are obtained by adding the Sun velocity, including the local standard of rest $\boldsymbol{\Theta}_\odot$ and the peculiar velocity $u_\odot$

$$\begin{aligned}\boldsymbol{v}_{\rm L,gal} &= \boldsymbol{v}_{\rm L,hel} + \boldsymbol{\Theta}_\odot + \boldsymbol{u}_\odot\,,\\ \boldsymbol{v}_{\rm S,gal} &= \boldsymbol{v}_{\rm S,hel} + \boldsymbol{\Theta}_\odot + \boldsymbol{u}_\odot\,. \end{aligned} \tag{20}$$

We take the circular orbital speed at the Sun $\Theta_0 = (236 \pm 7)$ km/s and the peculiar velocity $\boldsymbol{u}_\odot = (18.5\,\hat{\boldsymbol{l}} + 7.1\,\hat{\boldsymbol{b}})$ km/s (Reid et al. 2019).

The average rotation of the disk is described by a rotation curve $\Theta(r)$ as a function of the Galactocentric distance r. Here we assume for simplicity a flat rotation curve with $\Theta(r) = \Theta_\odot$. The peculiar velocities are then

$$\begin{aligned}\boldsymbol{u}_{\rm L} &= \boldsymbol{v}_{\rm L,gal} - \boldsymbol{\Theta}(r_{\rm L})\,,\\ \boldsymbol{u}_{\rm S} &= \boldsymbol{v}_{\rm S,gal} - \boldsymbol{\Theta}(r_{\rm S})\,. \end{aligned} \tag{21}$$

The vector $\boldsymbol{\Theta}(r)$ is obviously tangent to a circle centered in the Galactic center with radius r. In our case, we have $r_{\rm L} = (6.81 \pm 0.12)$ kpc and $r_{\rm S} = (6.70 \pm 0.20)$ kpc. Finally, we obtain

$$\begin{aligned}\boldsymbol{u}_{\rm L} &= [(-17.30 \pm 3.92)\,\hat{\boldsymbol{l}} + (13.45 \pm 0.85)\,\hat{\boldsymbol{b}}]\,\mathrm{km/s}\,,\\ \boldsymbol{u}_{\rm S} &= [(-32.03 \pm 6.60)\,\hat{\boldsymbol{l}} + (-0.74 \pm 0.92)\,\hat{\boldsymbol{b}}]\,\mathrm{km/s}\,. \end{aligned} \tag{22}$$

Following the same approach for the W- model we obtain $\boldsymbol{u}_{\rm L} = [(-16.06 \pm 4.32)\,\hat{\boldsymbol{l}} + (-6.04 \pm 1.25)\,\hat{\boldsymbol{b}}]$ and $\boldsymbol{u}_{\rm S} = [(-46.41 \pm 3.93)\,\hat{\boldsymbol{l}} + (26.70 \pm 1.82)\,\hat{\boldsymbol{b}}]$. Now we are in a position to discuss the kinematics of the source and the lens using their peculiar velocities with respect to the average disk rotation. For model C+, the components along the Galactic latitude are relatively small, confirming that the two objects share kinematic properties with the Galactic Disk. The negative sign in the longitudinal component indicates that both objects seem to be moving away from the Galactic center and/or at a lower velocity with respect to the assumed average rotation $\theta(r)$. In any case, the magnitude of this component is not too large, considering the uncertainties in Galactic rotation. From the low values of the components of the peculiar velocities we may conclude that both the lens and the source follow the average rotation of the Galactic disk very closely and can thus be assigned to the thin disk component, from a kinematic point of view. The results obtained for the wide model W- also describe stars that seem to be moving away from the Galactic center. The different signs for the components along the Galactic latitude are due to the different direction of the parallax that occurs in the two cases. But even in this configuration, we obtain objects with typical properties of Galactic disk stars. The higher peculiar velocity of the source star may be consistent with a more evolved object, as suggested by its color-magnitude position above the main sequence.

6. Conclusions

We analyzed the microlensing event Gaia21blx, discovered by Gaia and densely observed by the OMEGA collaboration. Careful modeling leads to four degenerate solutions with a good measure of the finite-source effect and a sub-optimal measure of parallax. The microlensing models have been complemented by the

information provided by Gaia. In particular, we have assumed that the parallax and the proper motion measured by Gaia are the flux-weighted averages of the parallaxes and proper motion of lens and source. Combining this assumption with constraints on the angular radius, the mass-luminosity relations and the microlensing parallax we have checked allowed lens masses and distances for our four models.

We find a better consistency for the two close-binary models, which correspond to a binary lens system located at 2.2 kpc. In this case, the lens is composed of a G star of 0.9 $M_\odot$ and a K star of 0.5 $M_\odot$. We infer that the source is most likely a subgiant F star located at 2.4 kpc. Both the lens and the source would belong to the thin Galactic disk and follow the average rotation rate very closely, lying in a region between the Sagittarius and the Centaurus arms. However, an alternative wide-binary model remains, although slightly disfavored by χ^2 and by the parallax constraint. In this case, the binary lens consists of a K-type star and an M dwarf located at 1.8 kpc, with the source at 2.6 kpc. In this case, the lens would be part of the stellar population of the Sagittarius arm, while the source would belong to the Centaurus arm.

Our conclusions could be confirmed by spectroscopic observations which might highlight the presence of lines from the source and at least the primary lens (since the secondary lens is probably a K-star it will be difficult to obtain its spectral lines), which contributes most of the blending. The novel approach introduced here for the analysis of Gaia21blx can be applied to similar events in which the blending is very high and fully attributed to the lens. Our assumption has led to a fully consistent physical picture from the point of view of photometry, astrometry and Galactic kinematics. The chances that random stars in the Galactic disk not involved in the microlensing event contribute to the blending are very low, while possible contamination by wide-binary companions of the source cannot be excluded by available data. This possibility could be tested by spectroscopic observations (with the ESO ESPRESSO (Pepe et al. 2021)) while high-resolution follow-up to separate the source and the lens is discouraged by the low relative proper motion.

Acknowledgements. This work has made use of the IAC-STAR Synthetic CMD computation code. IAC-STAR is supported and maintained by the IT department of the Instituto de Astrofísica de Canarias.
EB gratefully acknowledge support from NASA grant 80NSSC19K0291. **This research has made use of the NASA Exoplanet Archive, which is operated by the California Institute of Technology, under contract with the National Aeronautics and Space Administration under the Exoplanet Exploration Program.** This work has made use of data from the European Space Agency (ESA) mission *Gaia* (`https://www.cosmos.esa.int/gaia`), processed by the *Gaia* Data Processing and Analysis Consortium (DPAC, `https://www.cosmos.esa.int/web/gaia/dpac/consortium`) and the Photometric Science Alerts Team (http://gsaweb.ast.cam.ac.uk/alerts). Funding for the DPAC has been provided by national institutions, in particular the institutions participating in the *Gaia* Multilateral Agreement. This work makes use of observations from the Las Cumbres Observatory global telescope network. YT acknowledges the support of DFG priority program SPP 1992 "Exploring the Diversity of Extrasolar Planets" (TS 356/3-1). RFJ acknowledges support for this project provided by ANID's Millennium Science Initiative through grant ICN12_009, awarded to the Millennium Institute of Astrophysics (MAS), and by ANID's Basal project FB210003. This work is supported by Polish MNiSW grant DIR/WK/2018/12 and European Union's Horizon 2020 research and innovation program under grant agreement No. 101004719 (OPTICON-RadioNet Pilot, ORP). We also acknowledge support by the italian PRIN 2022J4H55R - Detection of Earth-like ExoPlanets, CUP D53D23002590006. N.P.'s work was supported by Fundação para a Ciência e a Tecnologia (FCT) through the research grants UIDB/04434/2020 and UIDP/04434/2020.

References

Albrow, M., Beaulieu, J. P., Birch, P., et al. 1998, ApJ, 509, 687
An, J. H., Albrow, M. D., Beaulieu, J. P., et al. 2002, ApJ, 572, 521
Aparicio, A., & Gallart, C. 2004, AJ, 128, 1465
Bachelet, E., Zieliński, P., Gromadzki, M., et al. 2022, A&A, 657, A17
Barnes, T. G., Evans, D. S., & Moffett, T. J. 1978, MNRAS, 183, 285
Belokurov, V. A., & Evans, N. W. 2002, MNRAS, 331, 649
Bennett, D. P., Rhie, S. H., Udalski, A., et al. 2016, AJ, 152, 125
Bond, I. A., Abe, F., Dodd, R. J., et al. 2001, MNRAS, 327, 868
Bond, I. A., Udalski, A., Jaroszyński, M., et al. 2004, ApJ, 606, L155
Boyajian, T. S., van Belle, G., & von Braun, K. 2014, AJ, 147, 47
Bozza, V. 2010, MNRAS, 408, 2188
Bozza, V., Bachelet, E., Bartolić, F., et al. 2018, MNRAS, 479, 5157
Bozza, V., Khalouei, E., & Bachelet, E. 2021, MNRAS, 505, 126
Bozza, V., Dominik, M., Rattenbury, N. J., et al. 2012, MNRAS, 424, 902
Bramich, D. M. 2008, MNRAS, 386, L77
Bramich, D. M., Horne, K., Albrow, M. D., et al. 2013, MNRAS, 428, 2275
Brown, T. M., Baliber, N., Bianco, F. B., et al. 2013, PASP, 125, 1031
Calchi Novati, S., Gould, A., Udalski, A., et al. 2015, ApJ, 804, 20
Capitanio, L., Lallement, R., Vergely, J. L., Elyajouri, M., & Monreal-Ibero, A. 2017, A&A, 606, A65
Cassan, A., Ranc, C., Absil, O., et al. 2022, Nature Astronomy, 6, 121
Castro-Ginard, A., McMillan, P. J., Luri, X., et al. 2021, A&A, 652, A162
Davenport, J. R. A., West, A. A., Matthiesen, C. K., Schmieding, M., & Kobelski, A. 2006, PASP, 118, 1679
de Bruijne, J. H. J., Allen, M., Azaz, S., et al. 2015, A&A, 576, A74
Dominik, M. 1999, A&A, 349, 108. https://arxiv.org/abs/astro-ph/9903014https://arxiv.org/abs/astro-ph/9903014
Dominik, M., & Sahu, K. C. 2000, ApJ, 534, 213
Dominik, M., Jørgensen, U. G., Rattenbury, N. J., et al. 2010, Astronomische Nachrichten, 331, 671
Drew, J. E., Gonzalez-Solares, E., Greimel, R., et al. 2014, MNRAS, 440, 2036
Einstein, A. 1936, Science, 84, 506
Fukui, A., Gould, A., Sumi, T., et al. 2015, ApJ, 809, 74
Gaia Collaboration, Prusti, T., de Bruijne, J. H. J., et al. 2016, A&A, 595, A1
Gaudi, B. S. 2012, Annual Review of Astronomy and Astrophysics, 50, 411
Girardi, L., Bressan, A., Bertelli, G., & Chiosi, C. 2000, A&AS, 141, 371
Gould, A. 2000, ApJ, 542, 785
—. 2004, ApJ, 606, 319, doi: http://doi.org/10.1086/38278210.1086/382782
Gould, A. 2008, in Manchester Microlensing Conference, ed. E. Kerins, S. Mao, N. Rattenbury, & L. Wyrzykowski, 38
Gould, A., & Loeb, A. 1992, ApJ, 396, 104
Gould, A., Udalski, A., Monard, B., et al. 2009, ApJ, 698, L147
Griest, K., & Safizadeh, N. 1998, ApJ, 500, 37
Herald, A., Udalski, A., Bozza, V., et al. 2022, A&A, 663, A100
Hodgkin, S. T., Breedt, E., Delgado, A., et al. 2021, Transient Name Server Discovery Report, 2021-890, 1
Jabłońska, M., Wyrzykowski, Ł., Rybicki, K. A., et al. 2022, A&A, 666, L16
Jordi, C., Gebran, M., Carrasco, J. M., et al. 2010, A&A, 523, A48
Kim, S.-L., Lee, C.-U., Park, B.-G., et al. 2016, Journal of Korean Astronomical Society, 49, 37
Klüter, J., Bastian, U., Demleitner, M., & Wambsganss, J. 2022, AJ, 163, 176
Kruszyńska, K., Wyrzykowski, Ł., Rybicki, K. A., et al. 2022, A&A, 662, A59
Lagarde, N., Robin, A. C., Reylé, C., & Nasello, G. 2017, A&A, 601, A27
Lagarde, N., Reylé, C., Robin, A. C., et al. 2019, A&A, 621, A24
Lam, C. Y., Lu, J. R., Udalski, A., et al. 2022, ApJ, 933, L23
Liebig, C., D'Ago, G., Bozza, V., & Dominik, M. 2015, MNRAS, 450, 1565
Lindegren, L. 2018
Malkov, O., Kovaleva, D., Zhukov, A., & Dluzhnevskaya, O. 2022, Ap&SS, 367, 37
Mao, S. 2012, Research in Astronomy and Astrophysics, 12, 947
Mao, S., & Di Stefano, R. 1995, ApJ, 440, 22
McCully, C., Volgenau, N. H., Harbeck, D.-R., et al. 2018, in Society of Photo-Optical Instrumentation Engineers (SPIE) Conference Series, Vol. 10707, Software and Cyberinfrastructure for Astronomy V, ed. J. C. Guzman & J. Ibsen, 107070K
McGill, P., Smith, L. C., Evans, N. W., Belokurov, V., & Smart, R. L. 2018, MNRAS, 478, L29
Miyake, N., Udalski, A., Sumi, T., et al. 2012, ApJ, 752, 82
Montegriffo, P., De Angeli, F., Andrae, R., et al. 2023, A&A, 674, A3
Mróz, P., Udalski, A., & Gould, A. 2022, ApJ, 937, L24
Olmschenk, G., Bennett, D. P., Bond, I. A., et al. 2023, The Astronomical Journal, 165, 175
Paczyński, B. 1986, ApJ, 304, 1
Pepe, F., Cristiani, S., Rebolo, R., et al. 2021, A&A, 645, A96
Raghavan, D., McAlister, H. A., Henry, T. J., et al. 2010, ApJS, 190, 1
Ranc, C., Cassan, A., Albrow, M. D., et al. 2015, A&A, 580, A125
Refsdal, S. 1966, MNRAS, 134, 315
Reid, M. J., Menten, K. M., Brunthaler, A., et al. 2019, ApJ, 885, 131

Riello, M., De Angeli, F., Evans, D. W., et al. 2021, A&A, 649, A3
Rybicki, K. A., Wyrzykowski, Ł., Klencki, J., et al. 2018, MNRAS, 476, 2013
Rybicki, K. A., Wyrzykowski, Ł., Bachelet, E., et al. 2022, A&A, 657, A18
Sahu, K. C., Anderson, J., Casertano, S., et al. 2022, The Astrophysical Journal, 933, 83
Shvartzvald, Y., Udalski, A., Gould, A., et al. 2015, ApJ, 814, 111
Skottfelt, J., Bramich, D. M., Hundertmark, M., et al. 2015, A&A, 574, A54
Skowron, J., Udalski, A., Gould, A., et al. 2011, ApJ, 738, 87
Street, R. A., Bachelet, E., Tsapras, Y., et al. 2024, ROME/REA: Three-year, Tri-color Timeseries Photometry of the Galactic Bulge. https://arxiv.org/abs/2403.05987https://arxiv.org/abs/2403.05987
Sumi, T., Abe, F., Bond, I. A., et al. 2003, ApJ, 591, 204
Tsapras, Y. 2018, Geosciences, 8, 365
Tsapras, Y., Street, R., Horne, K., et al. 2009, Astronomische Nachrichten, 330, 4
Udalski, A. 2003, ApJ, 590, 284
van Hamme, W. 1993, AJ, 106, 2096
Wyrzykowski, Ł., Kostrzewa-Rutkowska, Z., Skowron, J., et al. 2016, MNRAS, 458, 3012
Wyrzykowski, Ł., Mróz, P., Rybicki, K. A., et al. 2020, A&A, 633, A98
Wyrzykowski, Ł., Kruszyńska, K., Rybicki, K. A., et al. 2023, A&A, 674, A23
Xia, F., Ren, S., & Fu, Y. 2008, Ap&SS, 314, 51
Yee, J. C., Shvartzvald, Y., Gal-Yam, A., et al. 2012, ApJ, 755, 102

[1] Dipartimento di Fisica E.R. Caianiello, Università di Salerno, Via Giovanni Paolo II 132, I-84084, Fisciano, Italy
[2] Istituto Nazionale di Fisica Nucleare, Sezione di Napoli, I-80126, Napoli, Italy
[3] Astronomisches Rechen-Institut, Zentrum für Astronomie der Universität Heidelberg (ZAH), 69120 Heidelberg, Germany
[4] Las Cumbres Observatory, 6740 Cortona Drive, Suite 102,93117 Goleta, CA, USA
[5] University of St Andrews, Centre for Exoplanet Science, School of Physics & Astronomy, North Haugh, St Andrews, KY16 9SS, United Kingdom
[6] Millennium Institute of Astrophysics MAS, Nuncio Monsenor Sotero Sanz 100, Of. 104, Providencia, Santiago, Chile
[7] Instituto de Astrofísica, Facultad de Física, Pontificia Universidad Católica de Chile, Av. Vicuña Mackenna 4860, 7820436 Macul, Santiago, Chile
[8] Institut d'Astrophysique de Paris, Sorbonne Université, CNRS, UMR 7095, 98 bis bd Arago, F-75014 Paris, France
[9] IPAC, Mail Code 100-22, Caltech, 1200 E. California Blvd., Pasadena, CA 91125 USA
[10] Astronomical Observatory, University of Warsaw, Al. Ujazdowskie 4, 00-478 Warszawa, Poland
[11] Department of Particle Physics and Astrophysics, Weizmann Institute of Science, Rehovot 76100, Israel
[12] Institute of Astronomy, Faculty of Physics, Astronomy and Informatics, Nicolaus Copernicus University in Toruń, Grudziądzka 5, 87-100 Toruń, Poland
[13] Centre for ExoLife Sciences, Niels Bohr Institute, University of Copenhagen, Øster Voldgade 5, 1350 Copenhagen, Denmark
[14] Department of Physics, Isfahan University of Technology, Isfahan, Iran
[15] Astronomy Research Center, Research Institute of Basic Sciences, Seoul National University, 1 Gwanak-ro, Gwanak-gu, Seoul 08826, Korea
[16] Instituto de Astrofísica e Ciências do Espaço , Universidade de Coimbra , 3040-004 Coimbra,Portugal
[17] Unidad de Astronomía, Universidad de Antofagasta, Av. Angamos 601, Antofagasta, Chile
[18] Department of Physics, Sharif University of Technology, PO Box 11155-9161 Tehran, Iran
[19] Universidad Católica de la Santísima Concepción, Concepcion, Chile
[20] Centre for Electronic Imaging, Department of Physical Sciences, The Open University, Milton Keynes, MK7 6AA, UK
[21] Institute for Astronomy, University of Edinburgh, Royal Observatory,Edinburgh EH9 3HJ, UK
[22] University of Southern Denmark, Department of Physics, Chemistry and Pharmacy, SDU-Galaxy, Campusvej 55, 5230 Odense M, Denmark